Applied Surface Science 257 (2011) 10045–10051

Contents lists available at ScienceDirect

Applied Surface Science

journal homepage: www.elsevier.com/locate/apsusc

Structural characterization of supported nanocrystalline ZnO thin films prepared by dip-coating

J.R. Casanova [a], E.A. Heredia [a,*], C.D. Bojorge [a], H.R. Cánepa [a], G. Kellermann [b], A.F. Craievich [c]

[a] CITEDEF-CINSO-CONICET Centro de Investigaciones en Sólidos, Juan B. de La Salle 4397, B1603ALO, Villa Martelli, Buenos Aires, Argentina
[b] Departamento de Física, Universidade Federal do Paraná, Curitiba, PR, Brazil
[c] Instituto de Física, Universidade de São Paulo, Cidade Universitária, São Paulo, SP, Brazil

ARTICLE INFO

Article history:
Received 21 December 2010
Received in revised form 28 June 2011
Accepted 28 June 2011
Available online 5 July 2011

Keywords:
ZnO
Nanostructured thin films
XR
GISAXS

ABSTRACT

Nanocrystalline ZnO thin films prepared by the sol–gel dip-coating technique were characterized by grazing incidence X-ray diffraction (GIXD), atomic force microscopy (AFM), X-ray reflectivity (XR) and grazing incidence small-angle X-ray scattering (GISAXS). The structures of several thin films subjected to (i) isochronous annealing at 350, 450 and 550 °C, and (ii) isothermal annealing at 450 °C during different time periods, were characterized. The studied thin films are composed of ZnO nanocrystals as revealed by analysing several GIXD patterns, from which their average sizes were determined. Thin film thickness and roughness were determined from quantitative analyses of AFM images and XR patterns. The analysis of XR patterns also yielded the average density of the studied films. Our GISAXS study indicates that the studied ZnO thin films contain nanopores with an ellipsoidal shape, and flattened along the direction normal to the substrate surface. The thin film annealed at the highest temperature, $T = 550$ °C, exhibits higher density and lower thickness and nanoporosity volume fraction, than those annealed at 350 and 450 °C. These results indicate that thermal annealing at the highest temperature (550 °C) induces a noticeable compaction effect on the structure of the studied thin films.

1. Introduction

ZnO nanopowders and thin films exhibit a number of interesting properties for varistors [1] in ceramic technology and as sensor element in gas sensor devices [2]. The band-gap and high exciton energies of ZnO make this material adequate for applications to luminescent devices operating in UV and visible. ZnO thin films are used as a part of pressure transducers and acusto-optic devices due to their piezoelectric properties and as window electrodes for solar cells because of they are transparent conductive films [3–7].

Several applications of the studied material require that the as-deposited films, which exhibit low density and amorphous porous structure, be transformed into final films with nanocrystalline structure and high density. Alternatively, the highly accessible porosity observed in ZnO films before compaction processes is an interesting feature due to their related catalytic photovoltaic and photonic properties [8]. This feature together with the inherently reduced dimensions of the thin films favour the fast diffusion of the analyte through the heterostructured interface [9]. Also, by varying the porosity and dopant concentration of the ZnO films, gas-sensing properties and response time can be tuned. Highly porous film sensors have a high sensitivity and longer response time [10].

This work aims at studying the structure of nanocrystalline ZnO thin films deposited on silica glass plates by the sol–gel dip-coating technique and subjected to either isochronous or isothermal high temperature annealing. The characterization of the ZnO thin films is performed by X-ray diffraction at grazing angles (GIXD), atomic force microscopy (AFM), X-ray reflectivity (XR) and grazing incidence small-angle X-ray scattering (GISAXS).

2. Experimental

2.1. Sample preparation

The precursor solution used to obtain the ZnO thin films is composed of zinc acetate dihydrate dissolved in absolute ethanol, distilled water and acetic acid [11,12]. This solution was stirred at 65 °C under reflux during one hour until a homogeneous and transparent solution was obtained. The colloidal solution was deposited on amorphous SiO_2 flat substrates by dip-coating with a withdrawal speed of 10 cm/min and subsequently dried at room temperature. The same dip-coating procedure was repeated 6 times for each studied sample.

In order to eliminate the organic part of the precursor, the as-deposited thin films were subjected to annealing at different

* Corresponding author. Tel.: +54 11 4709 8100; fax: +54 11 4709 8228.
E-mail address: eheredia@citedef.gob.ar (E.A. Heredia).

0169-4332/$ – see front matter © 2011 Elsevier B.V. All rights reserved.
doi:10.1016/j.apsusc.2011.06.136

temperatures. Results of Differential Scanning Calorimetry (DSC) and Thermogravimetric Analyses (TGA) not reported here indicated that the sample mass remains practically constant above 350 °C. This demonstrates that at this temperature, in heating cycles, the residual organic parts of the thin films are fully eliminated. Final 3 h isochronous annealing was performed on three different samples held at 350, 450 and 550 °C, respectively. Other set of samples submitted to isothermal annealing at 450 °C during 1, 3 and 8 h, respectively, were also studied. As we will see, these annealing procedures transform the initially amorphous and organo-inorganic structure of the as-deposited thin films into thin films composed of nanometric ZnO crystals.

2.2. Structural characterization of the ZnO thin films

The crystallographic structure of the polycrystalline ZnO thin films studied here – after high temperature annealing – was characterized by using grazing incidence X-ray diffraction (GIXD). The X-ray diffraction patterns were obtained by using a PW 3710 Philips diffractometer with Cu-Kα radiation. The diffraction patterns were obtained keeping constant the incidence angle, $\alpha_i = 1^\circ$. The average sizes of the ZnO crystallites in different films were determined by applying Scherrer equation [13].

The root mean square (RMS) surface roughness parameter, η, and the thickness of the thin films, d, were determined by AFM. These results derived from AFM analysis are named as η_{AFM} and d_{AFM}, respectively. The film thickness was determined by scratching it with a steel cutting tool and then measuring the magnitude of the edge. The image processing was performed by using the WSxM software [14].

In order to characterize the nanostructure of the studied thin films, synchrotron XR and GISAXS measurements were performed using the D10A-XRD2 beamline of LNLS, Campinas, Brazil. Experiments were carried out using a monochromatic X-ray with a wavelength 0.15498 nm. The X-ray detectors for XR and GISAXS measurements were a fast scintillator and an imaging plate, respectively. XR measurements were performed using the α–2α step scanning procedure while GISAXS measurements were carried out on an immobile flat sample keeping a constant incidence angle, α_i, slightly larger than the critical angle for total reflection ($\alpha_i = 0.315^\circ$). Because of the shadow produced by the substrate in GISAXS measurements, only the upper half of the total scattering pattern was recorded.

The analysis of the recorded XR patterns allowed us to determine the average density, ρ, thickness, d_{XR}, and RMS roughness parameter, η_{XR}, of the studied thin films. Modelled functions were fitted to the whole XR experimental spectra by applying Parratt32-1.6 software [15]. This package is based on the recursive Parratt formalism [16] and on the Nevot–Croce model for roughness determination [17]. As will be shown in Section 3.3, the average mass density of deposited films being much lower than homogeneous ZnO, suggested the presence of a significant nanoporosity in the deposited layers.

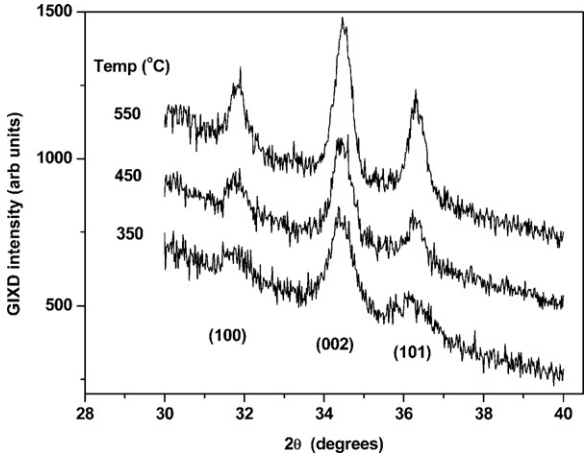

Fig. 1. GIXD patterns corresponding to ZnO thin films annealed during 3 h at 350, 450 and 550 °C.

The GISAXS technique was applied to the characterization of the internal nanoporosity inside the thin films. The analysis of GISAXS curves was carried out by applying the IsGisaxs 2.6 software package [18,19] using the distorted wave Born approximation (DWBA) that takes into account the reflection–refraction effects at the surface of the substrate and considers the contrast variation produced by the pores as a first order perturbation.

3. Results and discussion

3.1. Grazing incidence X-ray diffraction

The GIXD patterns corresponding to ZnO thin films annealed during 3 h at 350, 450 and 550 °C are plotted in Fig. 1. The presence of well defined and wide Bragg peaks in the GIXD patterns indicated that the studied thin films are nanostructured materials. All Bragg peaks in the patterns displayed in Fig. 1 were indexed by assuming that the thin films are composed of ZnO nanocrystals with a cubic wurtzite structure similar to that of bulk ZnO.

Average sizes of the ZnO nanocrystals were determined – under the assumption of an isotropic shape – from the width of the strongest (0 0 2) Bragg peak. The average crystallite sizes determined from the (0 0 2) peak profile, after being corrected for instrumental effects, are 13, 16 and 20 nm for samples annealed at 350, 450 and 550 °C, respectively (Table 1).

3.2. Atomic force microscopy

Two AFM images corresponding to ZnO thin films, annealed during 3 h at 350 and 450 °C, are displayed in Fig. 2a and c, respectively. Visual examination of these images indicates the presence of clearly different roughness features. The roughness parameters, η_{AFM}, of these thin films – determined from a quantitative analysis of the

Table 1
Structural parameters of ZnO thin films submitted to different thermal annealing. ρ: mass density, d_{XR} and d_{AFM}: film thickness derived from XR and AFM, respectively, η_{XR} and η_{AFM}: roughness parameter derived from XR and AFM, respectively, v_p: nanopore volume fraction, υ: nanopore aspect ratio, $\langle R\rangle$: nanopore average radius, and σ_R: relative standard deviation of the lognormal radius distribution.

T (°C)	t (h)	Number of layers	ρ (g/cm^3)	d_{XR} (nm)	d_{AFM} (nm)	η_{XR} (nm)	η_{AFM} (nm)	$\langle D\rangle$ (nm)	v_p	υ	$\langle R\rangle$ (nm)	σ_R (nm)
350	3	1	3.76	19	17	6.4	5.6	13	0.33	0.94	4.87	1.54
450	1	2	3.50	15	20	4.4	3.3	–	0.37	0.75	5.10	2.07
	3	1	3.89	16	–	6.6	7.6	16	0.30	0.78	4.57	2.14
	8	2	3.57	18	23	4.9	5.1	–	0.36	0.80	4.58	2.01
550	3	1	4.12	13	–	5.2	6.9	20	0.26	0.75	5.14	1.98

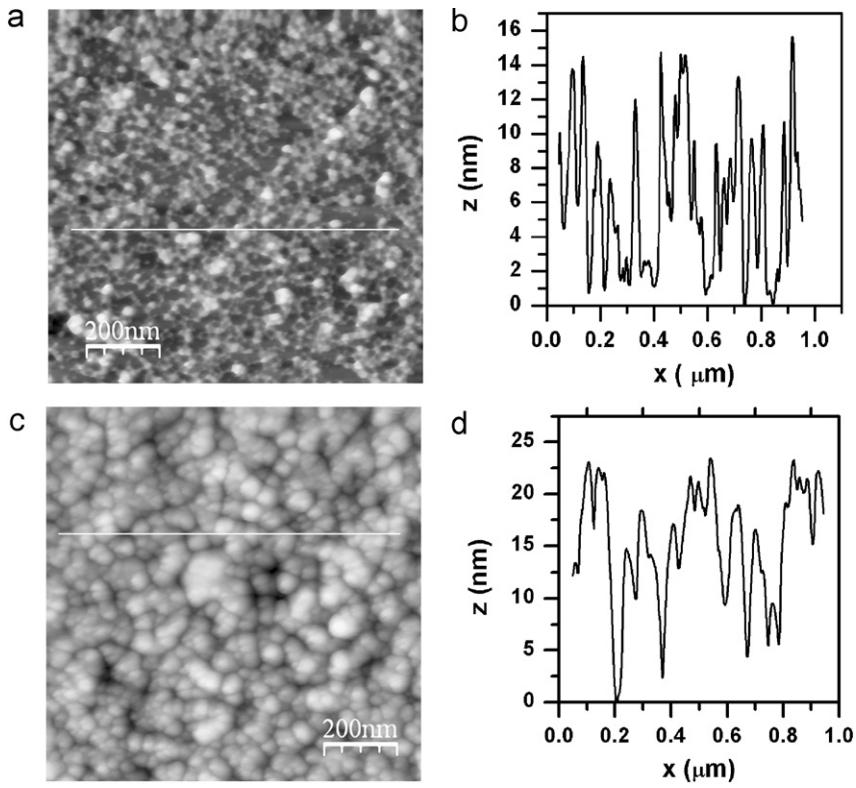

Fig. 2. (a) AFM micrograph of the surface of a ZnO thin film annealed during 3 h at 350 °C. (b) Height profile related to the surface shown in Fig. 2a. (c) AFM micrograph of a thin film annealed during 3 h at 450 °C. (d) Height profile related to the surface shown in Fig. 2c.

profiles plotted in Fig. 2b and d – are 5.6 and 7.6 nm, respectively (Table 1).

Fig. 3a and b displays two profiles from AFM images corresponding to thin films scratched with a steel cutting tool. In both height profiles, the grooves and damage produced on the substrate by the scratch are clearly evidenced. Accumulation of removed material is observed on several groove edges. The thicknesses of three films were estimated from deepness analysis of these grooves. The d_{AFM} values, reported in Table 1, range from 17 nm up to 23 nm.

3.3. X-ray reflectometry

XR patterns of the studied thin films are presented in Fig. 4a and b, each set of curves corresponding to isochronous and isothermal annealing procedures, respectively. The experimental X-ray reflectivity curves are plotted as functions of the grazing incidence angle α_i. The X-ray reflectivity is defined as $R(\alpha_i) = I(\alpha_i)/I_{max}$, $I(\alpha_i)$ being the X-ray intensity of the reflected beam and I_{max} the maximum of $I(\alpha_i)$ which occurs well below the critical α_c angle for total reflection. The intensity correction for low grazing angles due to the beam width and sample size was included [20].

The oscillations of the XR patterns expected at high α_i are not pronounced in any reflectivity curve. As a consequence, the thicknesses of the films – whose classical determination utilises the α values corresponding to the maxima and minima of the Kiessig fringes and applies a modified Bragg equation [20] – could not directly be determined. Instead, the thicknesses were estimated by fitting modelled functions to the whole experimental XR patterns. This procedure was performed by using the Parratt package [15], which was also applied to determine the roughness parameter of the thin film surfaces and substrate surface.

We have first tried to model the experimental $R(\alpha_i)$ function corresponding to all XR profiles by assuming a single average density for the whole thin film. This one-layer model led to XR profiles that fit well to all experimental $R(\alpha_i)$ curves except to the spectra corresponding to thin films annealed 1 and 8 h at 450 °C. In order to obtain a modelled $R(\alpha_i)$ with an acceptable fitting quality for these two particular thin films, an alternative two-layer model was assumed.

The main parameters obtained by the best fitting of the modelled functions to the experimental profiles are reported in Table 1. The second layer that was added at the bottom of the film to improve the fitting quality of the modelled function is very thin (thickness $d \approx 1$ nm). Therefore, for the samples to which the two-layer model was applied, we have reported in Table 1 only the total film thickness, the average density of the whole films and the external surface roughness.

The Nevot–Croce roughness factor [17] can be applied provided the condition $q_z\eta_{XR}/2 < 1$ or $\alpha_i \gg \underline{\alpha}_c$ – is obeyed (q_z being the component of the scattering vector normal to the surface) [21]. In our XR measurements, the roughness parameters of the ZnO thin films were in all cases rather large ($\eta_{XR} \sim 5.5$ nm). This implies that the fitting using Nevot–Croce roughness factor can be applied to the studied thin films only up to a maximum angle $\alpha_{max} = 0.25°$ and to very large α_i values. Since our XR measurements were performed in the $0.1 < \alpha_i < 1°$ range, the above conditions were only partially fulfilled. As a consequence we should consider the structure parameters derived from XR measurements (average density, thickness and roughness parameter) as subjected to not negligible errors.

The average mass densities reported in Table 1 are in all cases lower than the density of homogeneous ZnO ($\rho_{ZnO} = 5.61$ g/cm^3). This finding indicates that the studied ZnO thin films are porous. It is worth noticing that the densities calculated from the values of

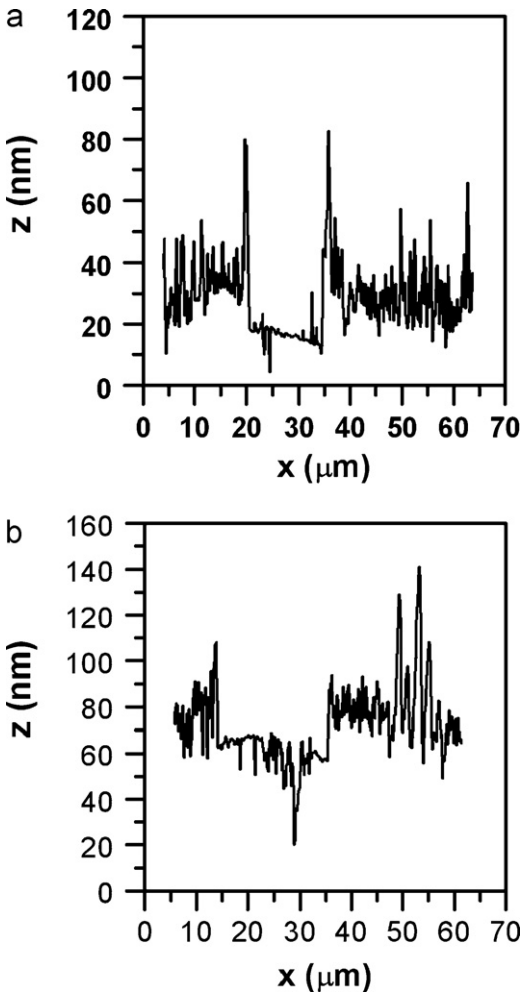

Fig. 3. Height profiles from AFM micrographs of ZnO films, scratched with a steel cutting tool, annealed during (a) 3 h at 350 °C, (b) 8 h at 450 °C.

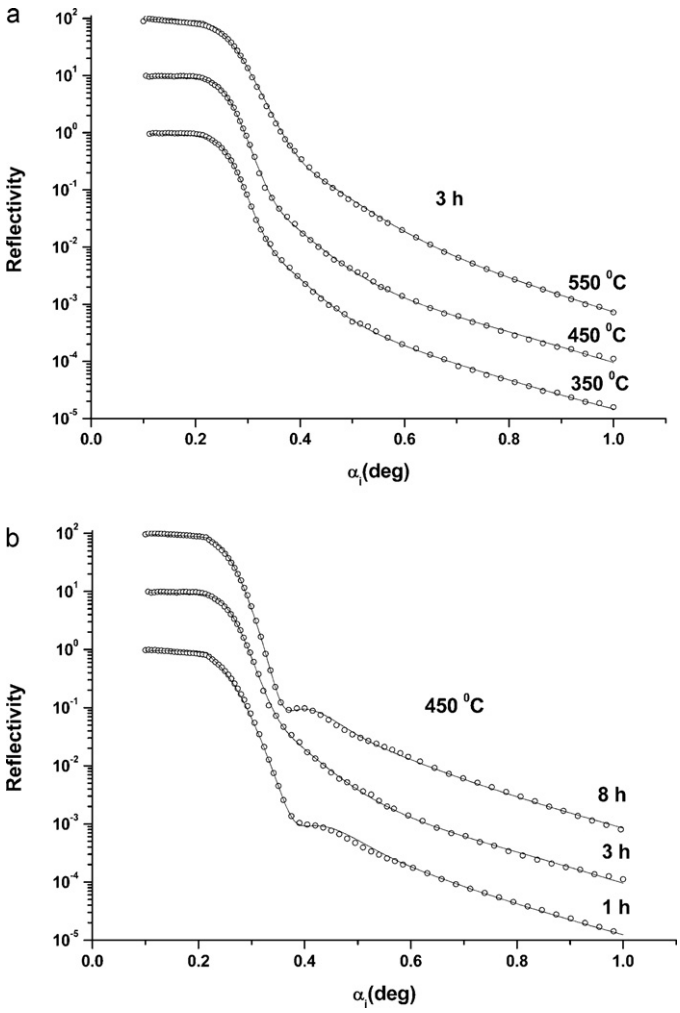

Fig. 4. X-ray reflectivity curves for all studied ZnO thin films for (a) isochronous 3 h annealing at the indicated temperatures, and (b) isothermal annealing at 450 °C during different time periods. The XR patterns are vertically shifted for clarity.

the critical angle [20] are somewhat lower than those obtained by the global fitting.

Under the assumption of a two density model for the studied ZnO thin films, – i.e. a homogeneous matrix in which empty pores are embedded – the porosity parameter (i.e. the volume fraction occupied by pores), v_p, can be determined by applying the following equation:

$$v_p = \frac{V_p}{V} = 1 - \frac{\rho}{\rho_{ZnO}} \quad (1)$$

where V_p and V are the total volume of nanopores and the volume of the thin film, respectively, and ρ and ρ_{ZnO} are the mass densities of the thin film and bulk crystalline ZnO, respectively. The volume fraction of the nanoporosity, v_p, reported in Table 1 ranges from 0.26 up to 0.37.

From the analysis of the XR pattern corresponding to the free surface of the flat amorphous SiO_2 substrate used for deposition, a roughness parameter $\eta_{XR} \approx 0.6$–0.8 nm was determined. On the other hand, the total thickness, d_{XR}, of the different samples ranges from 12.8 up to 18.3 nm. These thicknesses are approximately consistent with those independently derived from AFM measurements ($17\text{ nm} < d_{AFM} < 23\text{ nm}$). The differences between both results can be assigned to different areas probed by AFM and XR measurements and/or also to errors in the values of d_{XR} determined by XR. This error could be the consequence of a part of our fitting procedure that was performed outside the angular range of validity of Nevot–Croce formalism for films with high roughness [21].

Data reported in Table 1 indicate that the thin films annealed during 3 h at the highest temperature (550 °C) exhibit the highest density ($\rho = 4.12\text{ g/cm}^3$) and the lowest thickness ($d_{XR} = 12.8$ nm). The film roughness parameters η_{XR} take values within the 4.4–6.6 nm range, these values being similar to those obtained by AFM. The small differences between the roughness parameters determined by AFM and XR can also be assigned to the different areas probed by AFM and XR measurements and/or to deviations related to our Parratt fitting using the Nevot–Croce factor for roughness within an angular range out of the limits allowed for samples with a high roughness [21].

The results of the modelling of the X-ray reflectivity profiles that best fit to the experimental curves by applying Parratt32 indicate that, for thin films with a thickness $d = 15$ nm, a roughness parameter $\eta \approx 5.5$ nm is the upper limit above which oscillations in the reflectivity spectrum do not occur. Since the roughness parameter derived from our fitting procedure takes values close to the mentioned upper limit, we can understand why the experimental XR patterns associated to all thin films studied here exhibit reflectivity profiles without well-defined oscillations.

The results reported in Table 1 indicate that the average ZnO crystallite sizes determined from GIXD (0 0 2) profile for thin films annealed at 350 and 450 °C are 50% smaller and approxi-

mately equal, respectively, to the thin film thicknesses derived from XR fittings. However, in the particular case of the thin film annealed at 550 °C, the average crystallite size derived from GIXD is ⟨D⟩ = 20 nm, this value being clearly higher than the thin film thickness, d_{XR} = 13 nm. Even thought the GIXD geometry probes crystallite sizes along a direction that is not rigorously normal to the film surface, this finding obviously is unexpected. We have assigned this effect to a rather low precision in the determination of the thickness d_{XR} by applying Parratt fitting to our XR results. As it was mentioned above, this low accuracy is an expected consequence of the very high roughness of the studied film surfaces. Therefore one only can safely conclude that the average sizes of the ZnO nanocrystals are, in all cases, similar to the thin film thicknesses.

3.4. Grazing incidence small angle X-ray scattering

A typical GISAXS 2D pattern is displayed in Fig. 5a, while Fig. 5b shows the intensity profiles as a function of the modulus of the in-plane component of scattering vector q, defined as $q_{||} = (2\pi/\lambda)[(\cos\alpha_f \cos 2\theta - \cos\alpha_i)^2 + (\cos\alpha_f \sin 2\theta)^2]^{1/2}$ [19], λ being the X-ray wavelength, 2θ the horizontal scattering angle and α_f the angle between the scattered X-ray beam and the surface of the sample. Ten horizontal cuts of the imaging plate at different exit angles α_f are indicated in Fig. 5a for which the GISAXS 1D profiles were determined.

A model assuming the existence of spatially uncorrelated and spherical nanopores with different size distributions was firstly tried. We did not include in our GISAXS model eventual interference effects due to spatial correlation of the nanopores because the nanopore size distribution is very wide. In cases of very high size polydispersivity, the spatial correlation among nanoparticles (or nanopores) is reduced as compared to the case of a (monodisperse) set of nanoparticles or nanopores of equivalent sizes. Due to this argument and even thought the pore volume fraction is rather high, we have assumed, as an approximation, that interference effects are not significant and thus they can be neglected. However the modelled GISAXS curves determined assuming spherical nanoparticles did not fit well in any case to our experimental profiles.

We have assumed a second model consisting of spatially uncorrelated nanopores with a simple shape of ellipsoid of revolution embedded in a homogeneous ZnO nanocrystalline matrix. The radius of the ellipsoidal nanopores in the directions parallel to the film surface is defined as R, while υR is the radius corresponding to the direction normal to the sample surface, the aspect ratio υ being equal to 1 for spherical nanopores. It was also assumed that the nanopores have a radius distribution $N(R)$, with a single valued υ parameter for all nanopores. $N(R)$ was defined as a lognormal function [19], which was previously demonstrated to be a good approximation for other similar nanoporous materials [22,23]:

$$N(R) = \frac{N}{\sqrt{2\pi}R\log(\sigma/R_0)} \exp\left[-\frac{1}{2}\left(\frac{\log(R/R_0)}{\log(\sigma/R_0)}\right)^2\right] \quad (2)$$

where N is the total number of nanopores. The average nanopore radius ⟨R⟩ and the standard deviation σ_R of the radius distribution $N(R)$ were derived from the parameters R_0 and σ that define the lognormal function (Eq. (2)). It has been considered that such radius distribution is valid only up to a maximum R emerged from υR value equal to half the thickness of the thin films, thus the distribution functions are truncated, as it is shown in Fig. 5c.

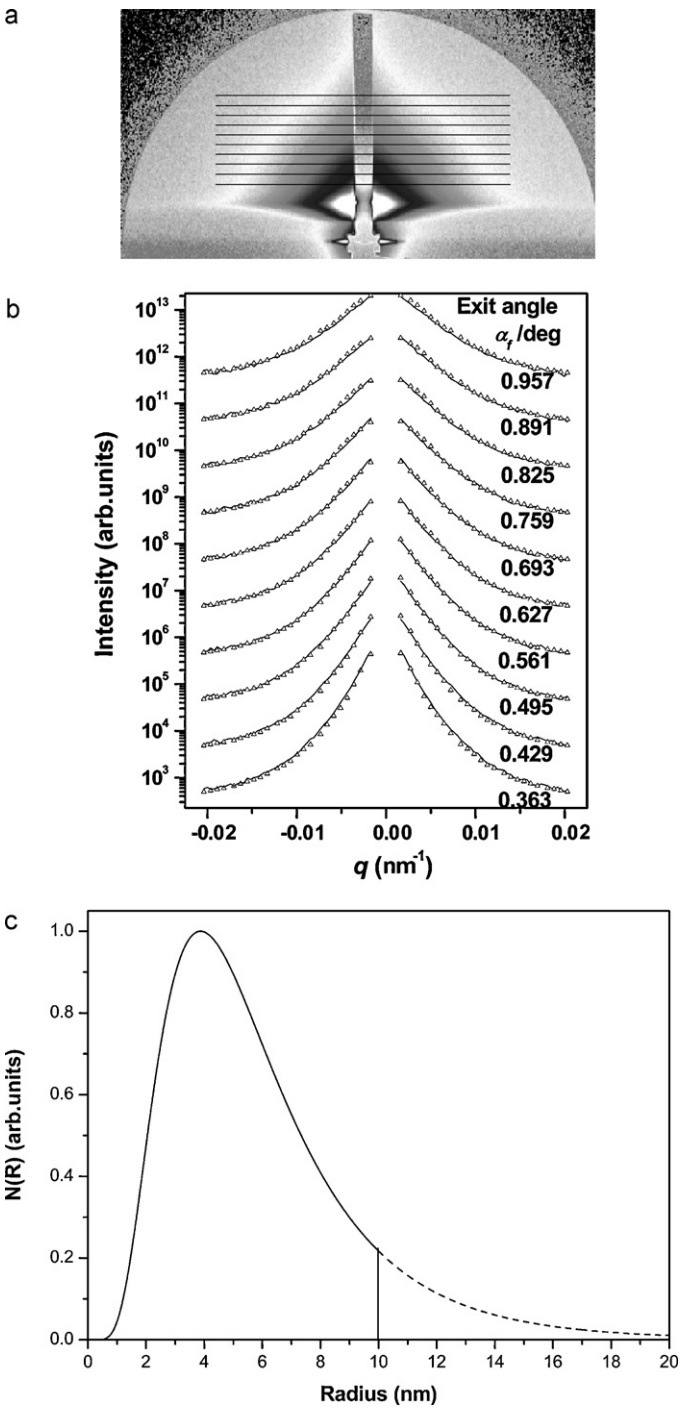

Fig. 5. (a) 2D GISAXS results displayed as an imaging plate picture for a ZnO thin film annealed during 1 h at 450 °C. (b) GISAXS curves corresponding to the horizontal cuts indicated in Fig. 5a. Solid lines are the modelled curves that exhibit the best fit to the experimental GISAXS curves. (c) Nanopore radius distribution derived form the GISAXS curves that best fitted to the experimental results.

The GISAXS intensity $I(q_{||}, \alpha_i, \alpha_f)$ produced by a spatially uncorrelated set of ellipsoidal empty nanopores with same aspect ratio υ, a size distribution given by $N(R)$, embedded in a layer deposited on a substrate, is written as [19]

$$I(q_{||}, \alpha_i, \alpha_f) \propto \int N(R)\left|\Phi(q_{||}, k_z^i, k_z^f, R, \upsilon)\right|^2 dR \quad (3)$$

where Φ is the effective scattering factor resulting from the coherent interference between four waves:

$$\begin{aligned}\Phi(q_{||}, k_z^i, k_z^f, R, \upsilon) &= T_1(\alpha_i)T_1(\alpha_f)\exp\left[-i(\tilde{k}_z^f - \tilde{k}_z^i)\delta\right] F(q_{||}, \tilde{k}_z^f - \tilde{k}_z^i, R, \upsilon) \\ &+ R_1(\alpha_i)T_1(\alpha_f)\exp\left[-i(\tilde{k}_z^f + \tilde{k}_z^i)\delta\right] F(q_{||}, \tilde{k}_z^f + \tilde{k}_z^i, R, \upsilon) \\ &+ T_1(\alpha_i)R_1(\alpha_f)\exp\left[-i(-\tilde{k}_z^f - \tilde{k}_z^i)\delta\right] F(q_{||}, -\tilde{k}_z^f - \tilde{k}_z^i, R, \upsilon) \\ &+ R_1(\alpha_i)R_1(\alpha_f)\exp\left[-i(-\tilde{k}_z^f + \tilde{k}_z^i)\delta\right] F(q_{||}, -\tilde{k}_z^f + \tilde{k}_z^i, R, \upsilon).\end{aligned} \quad (4)$$

$R_1(\alpha_{i,f})$ and $T_1(\alpha_{i,f})$ being the amplitudes of the upwards and downwards propagating waves, $\tilde{k}_z^i$ and $\tilde{k}_z^f$ are the perpendicular components of the refracted and scattered wave-vectors inside the layer and δ the average buried depth of nanopores. F is the form factor associated to an ellipsoid of revolution. The $T_1(\alpha_f)$ function gives rise to a maximum in the scattering intensity pattern at α_f values close to the critical angle of X-ray total reflection, the so called Yoneda peak.

The aspect ratio of the ellipsoidal nanopores, υ, the average radius nanopore $\langle R\rangle$ and the standard deviation of the nanopore radius distribution, σ_R, reported in Table 1 are determined from the $N(R)$ function (Eq. (2)) corresponding to the scattering intensity $I(q_{||}, \alpha_i, \alpha_f)$ (Eq. (3)) that exhibits the best fit to the different experimental GISAXS curves.

The thickness and refraction index of the studied ZnO thin films, derived from our experimental XR analyses, were used as input parameters to run the package IsGISAXS. The modelled GISAXS curves that exhibit the best fit to all profiles corresponding to the 10 horizontal lines shown in Fig. 5a, at different exit angle α_f, are indicated by solid lines in Fig. 5b. Fig. 5c displays the corresponding radius distribution functions $N(R)$ corresponding to the thin film annealed during 1 h at 450 °C.

The aspect ratios, υ, of nanopores reported in Table 1 for the samples studied here are all of them lower than 1, thus indicating that the shape of the nanopores can be seen as that of spheres flattened in the direction normal to the thin film surface, i.e. the nanopore shape is that of an oblate ellipsoid of revolution. The average radii $\langle R\rangle$ and the standard deviations σ_R of the ellipsoidal nanopores – resulting from the fitting procedure and corresponding to all studied samples – are also reported in Table 1.

The GISAXS curves related to the thin films under isothermal annealing at 450 °C do not show significant differences for increasing time periods, from 1 up to 8 h. In fact, the variation in the values of the average radius $\langle R\rangle$ corresponding to the different time periods are similar to their respective uncertainties, showing that a clear trend of the different structural parameters under isothermal annealing at 450 °C cannot not be inferred from our experimental results.

The GISAXS results corresponding to isochronous annealing at different temperatures reveal that the average lateral radius of the nanopores increases from 4.87 nm for annealing at 350 °C up to 5.14 nm at 550 °C, while the aspect ratio decreases from 0.94 down to 0.75 and the porosity volume fraction from 0.37 to 0.26 (Table 1). As reported in Table 1 the decreasing trend of the aspect ratio or flattening effect on the nanopores for increasing annealing temperatures is well correlated to the observed small thickness of the thin film and low volume fraction of nanopores for samples annealed at 550 °C as compared to samples annealing at 350 and 450 °C. If one compares the thicknesses and porosity fractions corresponding to thin films annealed at 350 and at 450 °C, the same temperature effect is not observed, thus indicating that the structure of ZnO thin films held up to 450 °C does not exhibit significant changes promoted by isothermal annealing during periods lasting up to 8 h.

On the other hand, the values of the nanopores radii are similar to the roughness parameter η derived from AFM and XR, thus indicating a clear correlation between the features of the surface roughness and the sizes of the internal nanopores in the studied thin films.

Finally it is worth mentioning that, in addition to the scattering intensity produced by nanopores, surface roughness also can contribute to the total GISAXS intensity. We have assumed here that the GISAXS intensity produced by nanopores is much stronger than the contribution from surface roughness. Because of this the contribution from surface roughness was not taken into account in our modelling procedure.

4. Conclusions

The structures of thin films composed of nanometric ZnO crystallites – prepared by dip-coating and supported by a flat silica substrate – were characterized by GIXD, AFM, XR and GISAXS. The structural characterization was performed on (i) samples subjected to isochronous annealing (3 h) at 350, 450 and 550 °C, and (ii) samples annealed during different time periods (1, 3 and 8 h) at 450 °C.

The thicknesses of the studied ZnO thin films range from 18.3 nm in the thin film annealed at 350 °C down to 12.8 nm in that annealed at 550 °C. The roughness parameter ranges from 4.4 up to 6.6 nm for the different samples without any clear correlation with the annealing temperature.

The studied thin films are polycrystalline and composed of ZnO nanocrystals with wurzite-like structure similar to the structure of bulk ZnO. The average nanocrystal sizes derived from GIXD ranges from 13 nm for thin films annealed at 350 °C up to 20 nm for those annealed at 550 °C. We can notice that the average sizes of the ZnO nanocrystals are similar to the thicknesses of the thin films. We have also noticed an opposite trend in the average nanocrystal sizes with respect to the film thickness for varying annealing temperatures. As a matter of fact, for increasing annealing temperatures, the average crystallite size increases while the thickness is reduced.

All studied ZnO thin films exhibit an internal nanoporous structure. GISAXS characterization indicates the presence of nanopores with an ellipsoidal shape flattened along the direction normal to the thin film surface. The average lateral radius $\langle R\rangle$ ranges from 4.57 nm up to 5.14 nm and does not exhibit a well defined trend for increasing annealing temperatures, while the aspect ratio decreases from 0.94 at 350 °C down to 0.75 at 550 °C.

The thin film annealed at the highest temperature, $T = 550$ °C, exhibits the highest density and average crystallite size and the lowest thickness, porosity volume fraction and pore aspect ratio, as compared to those annealed at 350 and 450 °C. These results indicate that the most efficient compaction occurs at the highest annealing temperature.

The decreasing trend of the aspect ratio or flattening of the nanopores annealed for increasing temperature – its minimum occurring at 550 °C – is well correlated to the observed reductions in thickness and in nanopore volume fraction. By comparing the values of the thicknesses, d, and porosity volume fractions, v_p, corresponding to the ZnO thin film annealed at 350 and 450 °C the same trend was not observed, thus indicating that isothermal annealing up to 8 h at 450 °C or below does not promote significant structural changes in the studied material.

Structural variations determined for ZnO thin films under isothermal annealing up to 8 h at 450 °C are weak and within the estimated experimental uncertainties. Therefore no clear conclusion about the effects of varying annealing periods during isothermal annealing could be drawn. In order to establish the time dependence of the structural variations under isothermal annealing of ZnO thin films, additional XR and GISAXS measurements at higher temperatures and/or longer time periods are required.

Acknowledgements

The authors acknowledge S. Ludueña, J. Bocchio and D. Lamas for their help regarding AFM, TGA-DSC and XRD experiments, respectively. They also thank LNLS, FAPESP, CAPES/SECyT, CNPq/CONICET, CNPq (PROSUL), ANPCyT, CONICET and YPF Foundation for funding support.

References

[1] X. Kang, T. Minjing, Z. Ming, W. Tiandiao, Microstructure and electrical properties of doped ZnO varistor nanomaterials , Solid State Phenomena 99–100 (2004) 127–132.
[2] X. Zhou, J. Zhang, T. Jiang, X. Wang, Z. Zhu, Humidity detection by nanostructured ZnO: a wireless quartz crystal microbalance investigation , Sensors and Actuators A 135 (2007) 209–214.
[3] R. Li, S. Yabe, M. Yamashita, S. Momose, S. Yoshida, S. Yin, T. Sato, UV-shielding properties of zinc oxide-doped ceria fine powders derived via soft solution chemical routes , Materials Chemistry and Physics 75 (2002) 39–44.
[4] M. Bredol, H. Althues, Luminescent nano-sized ZnS and ZnO particles , Solid State Phenomena 99–100 (2004) 19–24.
[5] Z. Wang, H.J. Li, Highly ordered zinc oxide nanotubules synthesized within the anodic aluminum oxide template , Applied Physics A 74 (2002) 201–203.
[6] H. Kind, H.Q. Yan, B. Messer, M. Law, P.D. Yang, Nanowire ultraviolet photodetectors and optical switches , Advanced Materials 14 (2002) 158–160.
[7] D.C. Look, Recent advances in ZnO materials and devices , Materials Science and Engineering B 80 (2001) 383–387.
[8] S. Lepoutre, B. Julián-López, C. Sanchez, H. Amenitsch, M. Linden, D. Grosso, Nanocasted mesoporous nanocrystalline ZnO thin films , Journal of Materials Chemistry 20 (2010) 537–542.
[9] C.S. Dandeneau, Y.H. Jeon, C.T. Shelton, T.K. Plant, D.P. Cann, B.J. Gibbons, Thin film chemical sensors based on p-CuO/n-ZnO heterocontacts , Thin Solid Films 517 (2009) 4448–4454.
[10] S.T. Shishiyanu, T.S. Shishiyanu, O.I. Lupan, Sensing characteristics of tin-doped ZnO thin films as NO_2 gas sensor , Sensors and Actuators B 107 (1) (2005) 379–386.
[11] L. Armelao, M. Fabrizio, S. Gialanella, F. Zordan, Sol-gel synthesis and characterisation of ZnO-based nanosystems , Thin Solid Films 394 (2001) 90–96.
[12] R.E. Marotti, C.D. Bojorge, E. Broitman, H.R. Cánepa, J.A. Badan, E.A. Dalchiele, A.J. Gellman, Characterization of ZnO and ZnO:Al thin films deposited by the sol-gel dip-coating technique , Thin Solid Films 517 (2008) 1077–1080.
[13] H.P. Klug, L.E. Alexander, X-ray Diffraction Procedures for Polycrystalline and Amorphous Materials , John Wiley & Sons, New York, 1974.
[14] I. Horcas, R. Fernandez, J.M. Gomez-Rodriguez, J. Colchero, J. Gomez-Herrero, A.M. Baro, Review of Scientific Instruments 78 (2007) 013705.
[15] C. Braun, Parratt 32 version 1.5 Software, Neutron Scattering Center , Hahn Maitner Institute, Berlin, 1999.
[16] L.G. Parratt, Surface studies of solids by total reflection of X-rays , Physical Review 95 (1954) 359–369.
[17] L. Nevot, P. Croce, Caractérisation des surfaces par réflexion rasante de rayons X. Application a l'etude du polissage de quelques verres silicates , Revue de Physique Appliquée 15 (1980) 761–779.
[18] R. Lazzari, IsGISAXS: a program for grazing-incidence small-angle X-ray scattering analysis of supported islands , Journal of Applied Crystallography 35 (2002) 406–421.
[19] R. Lazzari, IsGISAXS Software version 2.6, Institut des NanoSciences de Paris, Universités Pierre et Marie Curie et Denis Diderot, CNRS, Paris, France, 2006.
[20] J. Bolze, M. Ree, H.S. Youn, S. Chu, K. Char, Synchrotron X-ray reflectivity study on the structure of templated polyorganosilicate thin films and their derived nanoporous analogues , Langmuir 17 (2001) 6683–6691.
[21] R. Zhang, R. Itri, M. Caffrey, Membrane structure characterization using variable-period X-ray standing waves , Biophys. J. 74 (1990) 1924–1936.
[22] B. Lee, J. Yoon, W. Oh, Y. Hwang, K. Heo, K.S. Jin, J. Kim, K. Woo Kim, M. Ree, In-situ grazing incidence small angle X-ray scattering studies on nanopore evolution in low-k organosilicate dielectric thin films , Macromolecules 38 (2005) 3395–3405.
[23] T. Sun, S. Donthu, M. Sprung, K. D'Aquila, Z. Jiang, A. Srivastava, J. Wang, V. Dravid, Effect of Pd doping on microstructure and gas sensing performance of nanoporous SnO_x thin films , Acta Materialia 57 (2009) 1095–1104.